Phase and structural characterization of $Sr_2Nb_2O_7$ and $SrNbO_3$ thin films grown via pulsed laser ablation in O_2 or N_2 atmospheres

K.R. Balasubramaniam[a], Y. Cao[a], N. Patel[a], S. Havelia[a], P.J. Cox[a], E.C. Devlin[a], E.P. Yu[a], B.J. Close[a], P.M. Woodward[b], P.A. Salvador[a],*

[a]*Department of Materials Science and Engineering, Carnegie Mellon University, Pittsburgh, PA 15213, USA*
[b]*Department of Chemistry, The Ohio State University, Columbus, OH 43210, USA*

Abstract

The influence of substrate temperature, process gas, deposition pressure, and substrate type on the phase selection, orientation/epitaxy, and growth morphology of thin films in the $SrNbO_y$ ($y \approx 3.0$ or 3.5) family was investigated. Pulsed laser deposited films (from a $Sr_2Nb_2O_7$ target) obtained in both oxygen and nitrogen atmospheres upon various substrates were characterized with X-ray diffraction, energy dispersive spectroscopy, atomic force microscopy, and transmission electron microscopy. In oxygen atmospheres, films adopted the (110)-layered perovskite structure of the target. Higher temperatures, lower pressures of oxygen, and use of (110)-oriented $SrTiO_3$ substrates lead to highly crystalline, epitaxial films of $Sr_2Nb_2O_7$. The use of nitrogen atmospheres resulted in cubic perovskite $SrNbO_3$ formation: epitaxial, textured, or polycrystalline films were obtained depending on the substrate; no nitrogen incorporation could be observed on the anion sublattice. On $SrTiO_3$, the cubic perovskite films followed a cube-on-cube epitaxy and planar defects were observed to occur on the (110) perovskite planes.
© 2008 Elsevier Inc. All rights reserved.

Keywords: Niobates; Layered perovskites; Laser deposition; Epitaxy

1. Introduction

The closed-shell transition-metal ions Zr^{4+}, Ti^{4+}, Nb^{5+}, and Ta^{5+} are electrically active in octahedral coordination environments, such as those found in perovskite compounds [1]. They exhibit interesting and useful dielectric, piezoelectric, ferroelectric, and optoelectronic properties [2–10]. Materials that are based on these cations also exhibit a rich variety in their crystallo-chemical behaviors, including their observed compositions, crystal structures, defect chemistry, and physical properties. Focusing on niobium-based compounds, this rich variation is reflected in the range of compositions that adopt perovskite-related structures, such as $A^{1+}Nb^{5+}O_3^{2-}$ [11], $A_{0.5}^{2+}Nb^{5+}O_3^{2-}$ [12], $A^{2+}Nb^{5+}O_2^{2-}N^{3-}$ [13], $A_5^{2+}Nb_4^{5+}O_{15}^{2-}$ [14], $A^{2+}Nb^{4+}O_3^{2-}$ [15], and $A_2^{2+}Nb_2^{5+}O_7^{2-}$ [16]. This family of niobium-based compounds is of interest because its members exhibit

ferroelectric [3,6,8,9], optoelectronic [4,5], photoactive [2,10], optical [17], and even conducting properties [16]. In this work, we investigate the thermodynamic and kinetic factors that control phase/orientation selection during thin film growth of materials where $A = Sr^{2+}$ and where the Sr:Nb ratio is ≈ 1 (see above list).

The air-stable phase in the system of interest has the composition $A_2^{2+}Nb_2^{5+}O_7^{2-}$ ($A = Sr$). This ferroelectric compound adopts a complex layered structure that is depicted in Fig. 1(c) and is closely related to the prototypical perovskite structure (ABX_3) depicted in Fig. 1(a) and (b). Fig. 1(a) highlights the arrangement of atoms in a single unit of the prototypical perovskite cell, including the octahedral B–X bonding, while Fig. 1(b) highlights the connectivity of the B–X polyhedra along the [110] direction of the ideal perovskite (p) structure. The chemical stacking sequence along the [110] direction in the simple perovskite is $-[X_2-ABX]-$. In the oxide ($X = O$) (110)-layered perovskites, one extra (110)-O_2 layer is inserted after m perovskite units. $Sr_2Nb_2O_7$ has a four-layer structure

---

*Corresponding author. Fax: +1 412 268 3113.

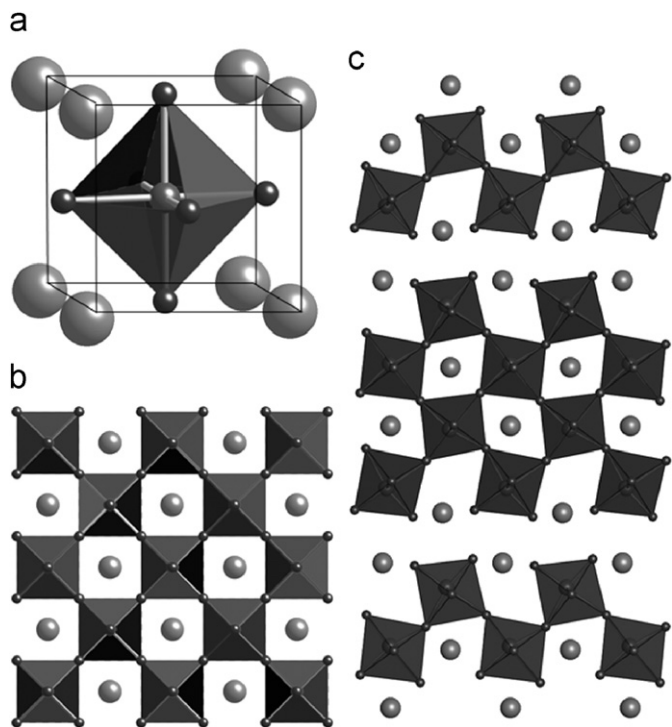*E-mail address:* paulsalvador@cmu.edu (P.A. Salvador).

Fig. 1. (a) Typical view of the perovskite (p) unit cell of an ABO_3 material. (b) Multiple unit cells of the same structure projected in the (001) plane, highlighting (in the vertical direction) the connectivity of the B–O octahedra and the stacking along a [110] direction. (c) Polyhedral representation of the complex [110]-layered perovskite oxide structure for an $A_2B_2O_7$ compound, projected in the (100) plane and highlighting the [010]. In all structures, the isolated spheres represent the A cations, the spheres at the apices of the octahedra represent O anions, and the spheres at the center of the octahedra represent B cations.

($m = 4$), which can be written as $-[O_2-\{O_2-ABO\}_4]-$ ($A =$ Sr, $B =$ Nb). This stacking generates the basic Nb–O topological framework of the structure shown in Fig. 1(c). It also implies that, to grow epitaxial films, (110)-oriented perovskite crystals will serve as the ideal substrate, because they have a good structural match to the layered ferroelectric. In reality, however, a significant number of atoms displace away from the positions generated by this simplified stacking. In the layered perovskite $A_2^{2+}B_2^{5+}O_7^{2-}$, the A cations near the double O_2 layers have completely displaced from the ABO layers (along the b-axis) into the O_2 layers. A better description of the stacking sequence along the b-axis in the real structure would be $-[-AO_2-\{(AO_2-BO)-(O_2-ABO)_2-(O_2-BO)\}]-$. More importantly, another set of displacements of the A, B, and O atoms (along the [010]-axis) lead to the ferroelectric nature of this family of materials. In fact, similarly distorted variants of the basic structure are observed for $Sr_2Nb_2O_7$ [16], $Sr_2Ta_2O_7$ [18], and $La_2Ti_2O_7$ [19], all of which are ferroelectric.

In oxygen poor environments, $Sr^{2+}Nb^{4+}O_3^{2-}$ [20] and $Sr^{2+}Nb^{5+}O_2^{2-}N^{3-}$ [13] compounds, that adopt structures based on the prototypical ABX_3 cubic perovskite structure, compete in stability with the layered perovskite structure of $Sr_2Nb_2O_7$. $Sr^{2+}Nb^{4+}O_3^{2-}$ phase formation by reduction of

the Nb cation occurs in reducing, poorly-nitriding environments when the ratio of Sr:Nb is near unity. In oxygen-poor, highly-nitriding environments, however, the reduction of the Nb cation (to form $Sr^{2+}Nb^{4+}O_3^{2-}$) competes with the incorporation of N onto the anion sublattice (to form $Sr^{2+}Nb^{5+}O_2^{2-}N^{3-}$), which may lead to the formation of the oxynitride phase.

$Sr_2Nb_2O_7$ forms easily using normal ceramic preparation methods [16,21,22], including thin film methods [5,7,9,10]. In general, polycrystalline films were obtained in these previous investigations that focused on the integration of this compound with silicon. To our knowledge, however, there are no reports of the growth of $Sr_2Nb_2O_7$ using pulsed laser deposition, or using a (110)-perovskite substrate that is likely to produce epitaxial films. In fact, the only report of epitaxial films is by Ishitani and Kimura [4], who produced epitaxial waveguide films of $Sr_2Nb_2O_7$(010) on single crystal $Sr_2Ta_2O_7$(010) substrates using rf-sputtering. In this work we focused on the growth of epitaxial films of the (110)-layered perovskite $Sr_2Nb_2O_7$ on a (110)-oriented perovskite $SrTiO_3$.

The literature on the thin film growth of $SrNbO_3$ compounds is even sparser than the literature on the growth of $Sr_2Nb_2O_7$ films. Only few groups [20,23,24] have reported the growth of both the end members in the $SrNb_xTi_{1-x}O_3$ series of compounds. In these studies, $SrNbO_3$ and $SrTiO_3$ thin films were grown by pulsed laser deposition on $SrTiO_3$(100) substrates. Tomio et al. [20] found a mixture of (100)- and (110)-oriented $Sr_{0.95}NbO_3$ films on $SrTiO_3$(100) substrates. Both studies indicate that very low oxygen pressures of $< 10^{-5}$ Torr O_2 (compared to 10^{-3} Torr for $SrTiO_3$ growth) resulted in better films. In this work, we focused on the growth of $SrNbO_3$ on $SrTiO_3$(100) and $SrTiO_3$(110) substrates in nitrogen ambients at pressures more typical to oxide film growth: in the range of 10^{-3}–10^{-1} Torr. High-quality films should be obtainable at these pressures because the overall oxygen activity is still low in these ambients.

Preparation of the anion-substituted phases is another possibility during pulsed laser ablation in N_2 atmospheres, since the plasma–gas interactions may lead to cracking of the N_2 bond and to nitrogen incorporation in the growing film. In fact, nitride phases can form easily during PLD of a metal target in nitrogen environments [25]; hence one must be concerned with the formation of such materials while carrying out PLD from an oxide target in a nitrogen environment. Recently, $BaTaO_2N$ films were prepared in N_2/O_2 mixtures from oxynitride targets, but the phase formation was very sensitive to the gas mixture [26]. There are, however, no reports on the growth of $SrNbO_2N$ films.

2. Experimental

The oxide ablation target was synthesized via standard solid-state ceramic synthesis methods [27,28]. Nb_2O_5 (99.9985%) and $SrCO_3$ (99.994%) (obtained from Alfa Aesar), were weighed in the correct proportions and mixed

together and ground. The pellets were annealed at three different temperatures (for approximately 12 h each): first at 900 °C, then at 1200 °C, and finally at 1500 °C. The crystallinity of the sintered pellet was characterized using a Rigaku X-ray diffractometer; it was verified to be polycrystalline $Sr_2Nb_2O_7$. The $Sr_2Nb_2O_7$ pellet was then used as the target in the film deposition process.

Films were deposited on single crystal substrates obtained from a commercial vendor (Crystal GmbH, Berlin, Germany). Substrates included (100)- and (110)-oriented $SrTiO_3$, $(100)_{pc}$-oriented $LaAlO_3$ (pc indicating our use of a pseudocubic perovskite notation), and (100)- and (111)-oriented MgO. 5 mm × 5 mm coupons (which were cut from larger crystals using a diamond wire saw) were first ultrasonically cleaned in acetone and ethanol (each for 10 min). The $SrTiO_3$(100) substrates were etched in a 3:1 $HCl:HNO_3$ mixture for 4 min and rinsed using deionized water. All samples were then mounted to the PLD heater-plate using silver paste. This was followed by a thermal anneal in the PLD chamber; either for a few minutes at the deposition conditions or, for $SrTiO_3$(100), at 850 °C in 200 mTorr O_2 for 1 h.

PLD was carried out in a commercial deposition system (Neocera®, Maryland) using a KrF excimer laser operating at a wavelength of 248 nm [27]. The laser was pulsed at a rate of 3 Hz and the beam was focused to a spot size of 8 × 1 mm² at the target surface, yielding an energy density of $\approx 2 J/cm^2$ at the target. The chamber was pumped down to a base pressure of $\approx 10^{-6}$ Torr before the turbomolecular pump was throttled down to 40% of its power and the process gas (O_2 or N_2) was bled into the chamber through a leak valve. During deposition, the dynamic pressure was maintained between 1 and 300 mTorr via the leak valve. The heater was maintained at different temperatures, in the range of 700–900 °C, and the target to substrate distance was fixed at ≈ 60 mm.

The crystalline nature (phase, crystalline quality, and epitaxial relationship) of the films was characterized using both a Rigaku and a Philip's X'Pert X-ray diffractometers equipped with Cu$K\alpha$ radiation; normal θ–2θ scans were carried out on the former, while ω and ϕ scans were carried out on the latter [27,29]. Cross-sectional transmission electron microscopy (TEM) samples were prepared using standard techniques. Energy dispersive spectroscopy (EDS) was carried out on the TEM samples (in scanning (STEM) mode) to determine the composition of the film using an FEI Tecnai F20 field emission gun transmission electron microscope (FEGTEM) operated at 200 kV and equipped with a Gatan imaging filter.

3. Results and discussion

3.1. Growth in oxygen ambients

3.1.1. Growth on SrTiO₃(110) substrates

The diffraction patterns given in Fig. 2 correspond to films deposited at $T = 900$ °C for 30 min and at $p_{O_2} = $ (a)

300 mTorr O_2, (b) 200 mTorr O_2, (c) 100 mTorr O_2, (d) 10 mTorr O_2, and (e) 1 mTorr O_2. In all cases, at this temperature, $Sr_2Nb_2O_7$(010) films were obtained, but the intensity on all $(0k0)$ peaks was observed to increase at the lowest pressures, indicating improved crystalline character as the pressure decreased. The out-of-plane lattice parameter calculated from the (080) peak is 26.74 Å. This value agrees well with the value of 26.73 Å for the bulk $Sr_2Nb_2O_7$ material [16]. At higher pressures, a low intensity peak marked with an "*" is located to the left of the substrate's (110) reflection (they are convoluted with one another and it is best observed in Fig. 2(b), although shoulders exist in Fig. 2(a) and (c)). This low intensity peak is consistent with the (002) peak of $Sr_2Nb_2O_7$ indicating that at higher pressures a small fraction of the film adopts an alternate orientation.

Fig. 3 presents the X-ray diffraction patterns for $Sr_2Nb_2O_7$ films deposited at four different temperatures on $SrTiO_3$(110) substrates (all at a $p_{O_2} = 1$ mTorr for 30 min). The diffraction patterns given in the figure correspond to films deposited at $T = $ (a) 600 °C, (b) 700 °C, (c) 800 °C, and (d) 900 °C. For the films deposited at $T = 600$ and 700 °C, the only peaks observed correspond to $Sr_2Nb_2O_7$ in the (001)-orientation. For films deposited at $T = 800$ and 900 °C, one observes a decrease in the amount of (001)-oriented $Sr_2Nb_2O_7$ and an increase in the amount of (010)-oriented $Sr_2Nb_2O_7$. Additionally, films exhibit improved crystallinity at the highest temperature, as evinced by the increased number of $(0k0)$ peaks observed in the XRD pattern. Similar trends have been observed for
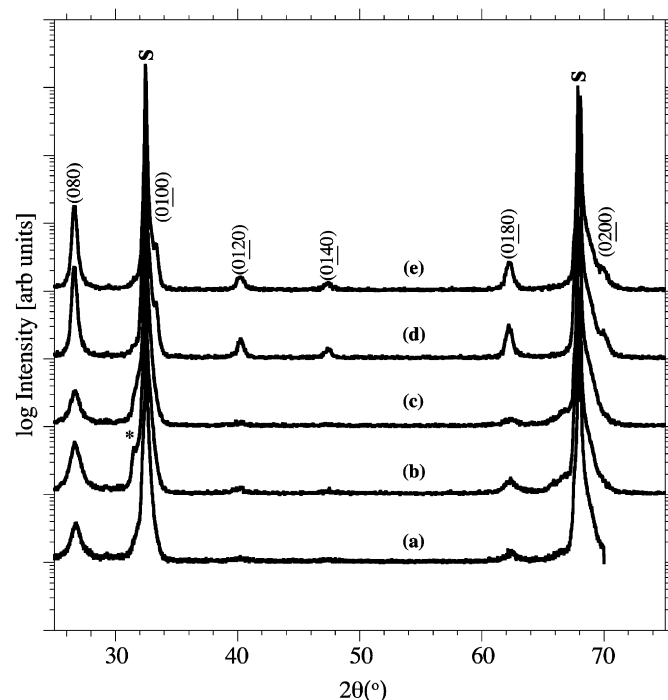
Fig. 2. XRD patterns of $Sr_2Nb_2O_7$ thin films grown on single crystal $SrTiO_3$(110) substrates at 900 °C at different oxygen pressures: (a) 300 mTorr, (b), 200 mTorr (c) 100 mTorr, (d) 10 mTorr, and (e) 1 mTorr O_2.

$Sr_2Nb_2O_7$ thin films prepared by other methods on other substrates; higher temperature heat treatments improve the proportion and quality of the (010)-orientated crystallites [5,7,9,10].

It is clear that for these ablation conditions, good quality, singly-textured $Sr_2Nb_2O_7(010)$ films are obtained for high temperatures (900 °C) and low oxygen pressures (1 mTorr). For our films, one expects that the (010)-orientation of the $Sr_2Nb_2O_7$ will align with the (110)-orientation of $SrTiO_3$, because the planes share the geometric arrangement of the perovskite (110)-planes. However, this is observed only at the highest temperature. For layered, anisotropic crystal structures, such as those for $Sr_2Nb_2O_7$ and the layered cuprate superconductors [30,31], high temperatures are required to align the chemically distinct layers parallel to the substrate. Diffusion is required both parallel to and normal to the substrate

surface plane in order for the layers to align properly, and diffusion normal to the substrate requires significantly more thermal energy. Therefore, higher temperatures lead to better b-axis alignment of the $Sr_2Nb_2O_7$ films. At lower temperatures where diffusion is limited, the b-axis cannot order properly out-of-plane and therefore lies in the plane and the (001)-orientation is observed. At 900 °C, the ability to order is observed to be a function of oxygen pressure, where higher pressures lead to an increase in the amount of the minor orientation having the b-axis in-plane, which is believed to arise from a relative decrease in diffusion with pressure.

3.1.2. AFM

Fig. 4 presents the AFM images for $Sr_2Nb_2O_7$ films deposited at three different temperatures of (a) 700 °C, (b) 800 °C, and (c) 900 °C on $SrTiO_3$(110) substrates (all at a $p_{O_2} = 1$ mTorr for 30 min). The surface morphology of all the films exhibits an island-like morphology, consistent with a columnar growth mode, with submicron size features and with high rms roughness values. The film deposited at 900 °C (Fig. 4(a)) exhibits a high rms roughness value of 68 Å. The rms roughness values for the film deposited at 800 °C have decreased to 50 Å. When the deposition temperature is lowered further, down to 700 °C, the flattest film surface morphology with rms roughness value of 22 Å is obtained. The increase in roughness values with temperature can be attributed to both higher diffusion rates and columnar (010)-oriented $Sr_2Nb_2O_7$ formation at the higher temperatures. The diffusion rates are lower at the lower temperatures and a flatter morphology is obtained.

3.1.3. Growth on $SrTiO_3(100)$ substrates

Fig. 5(a) shows the X-ray diffraction results of $Sr_2Nb_2O_7$ thin films grown on $SrTiO_3$(100) substrates at a substrate temperature of 900 °C and background oxygen pressure of 5 mTorr O_2 (other deposition parameters are similar to the films deposited on $SrTiO_3$(110) substrates; Fig. 5(b) is one such X-ray pattern). There is no clear evidence of any crystalline peaks from the film (the peaks marked s correspond to the substrate peaks) even at these high temperatures and low O_2 pressures. Similar growth conditions on $SrTiO_3$(110) substrates resulted in the facile
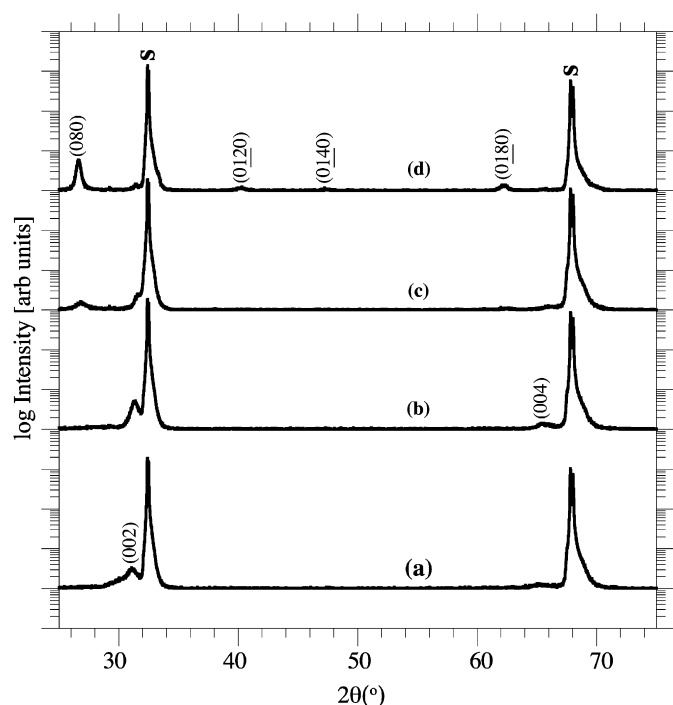

Fig. 3. XRD patterns of $Sr_2Nb_2O_7$ thin films grown on single crystal $SrTiO_3$(110) substrates in $p_{O_2} = 1$ mTorr and at (a) 600 °C, (b) 700 °C, (c) 800 °C, and (d) 900 °C.
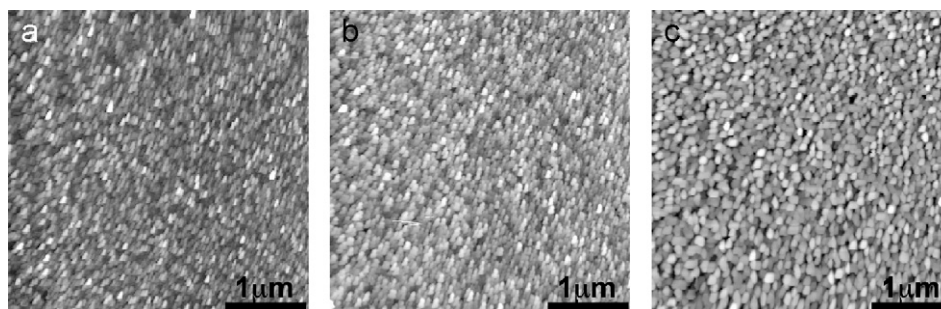

Fig. 4. AFM images of $Sr_2Nb_2O_7$ thin films grown on single crystal $SrTiO_3$(110) substrates in $p_{O_2} = 1$ mTorr and at (a) 700 °C, (b) 800 °C, and (c) 900 °C. the peak to valley gray scale and rms roughness values are (a) ≈ 33 nm and 2.2 nm, (b) ≈ 41.0 nm and 5.0 nm, and (c) ≈ 114 nm and 6.8 nm.
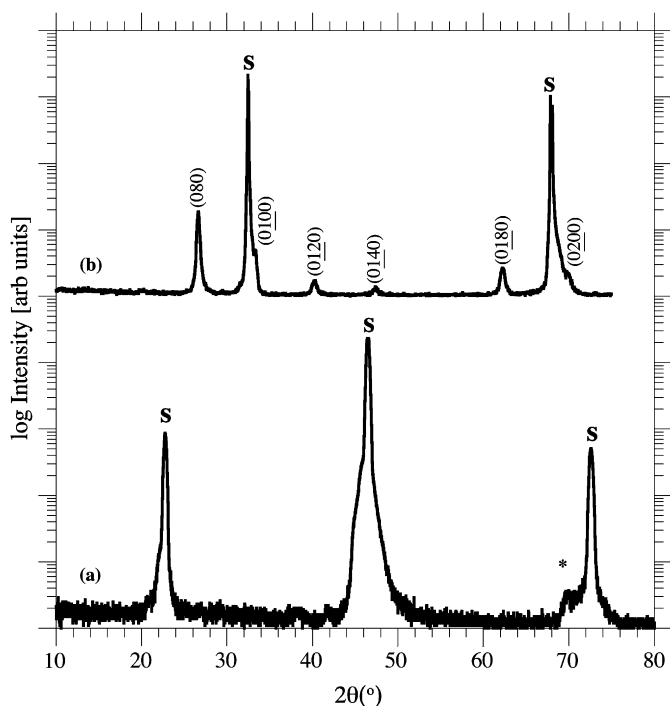
Fig. 5. XRD patterns of $Sr_2Nb_2O_7$ thin films grown in $p_{O_2} = 5$ mTorr and at 900 °C on (a) $SrTiO_3(110)$ and (b) $SrTiO_3(100)$ substrates.

attainment of $Sr_2Nb_2O_7$ thin films as the substrate surface is geometrically similar to the (010) plane of the layered perovskite. The (100) plane of $SrTiO_3$ on the other hand does not have any corresponding plane (geometrically similar) in the layered perovskite. Thus, it is observed that growth of crystalline $Sr_2Nb_2O_7$ thin films on $SrTiO_3(100)$ substrates is difficult as there is no geometrically similar plane between the film and the (100) plane of the perovskite substrate.

3.2. Growth in nitrogen ambients

From the results of the previous section we can conclude that niobium is stabilized in its pentavalent state even under low oxygen pressures of 1 mTorr O_2. In order to facilitate the reduction of niobium one needs to be at even lower O_2 pressures. This can be achieved by use of (i) extremely low pressures of O_2 or (ii) gases having very low partial pressures of oxygen (e.g., nitrogen). Tomio et al. [20] have studied the first possibility of obtaining $SrNbO_3$ in extremely low oxygen pressures ($\approx 10^{-5}$ Torr). Another possibility during the pulsed laser ablation in N_2 atmospheres is N_2 incorporation in the growing film leading to the formation of the oxynitride phase, $SrNbO_2N$, wherein there is no reduction of the Nb^{5+} cation. The results presented in this section demonstrate that nitrogen ambients promote the reduction of Nb^{5+} to Nb^{4+}.

Several substrates were chosen to explore the growth of the perovskite $SrNbO_3$. The first was the perovskite $SrTiO_3$ in both the (100) and (110) orientations, which allows for direct comparisons to be made to the $Sr_2Nb_2O_7$

films discussed above. The second was the perovskite $LaAlO_3(001)$, which allows us to understand the effect of strain, since the compressive lattice mismatch increases from -2.96% on $SrTiO_3(100)$ to -5.07% on $LaAlO_3(100)$. Finally, films were deposited on the (100) and (111) surfaces of the rock-salt MgO, which has a different structure and only provides semi-coherent interfaces. For a cube-on-cube type epitaxy, the lattice mismatch on MgO substrates is $\approx 4.45\%$.

3.2.1. XRD-phase identification

Fig. 6 gives the XRD patterns of films deposited in nitrogen ambient of $p_{N_2} = 50$ mTorr for 30 min at three temperatures and on two substrates. The temperatures of deposition were 800 °C in Fig. 6(a) and (d), 850 °C in Fig. 6(b) and (e), and 900 °C in Fig. 6(c) and (f). The diffraction patterns in Fig. 6(a)–(c) correspond to deposition on $SrTiO_3(100)$ substrates and in Fig. 6(d)–(f) correspond to films obtained on $SrTiO_3(110)$ substrates. The substrate peaks are marked s in all the patterns.

The pattern given in Fig. 6(a) exhibits no clear evidence for the existence of a crystalline perovskite film, having only a low-intensity diffuse peak near the (200) position ($2\theta = 44.91°$). An increase in the substrate temperature at these N_2 pressures of $p_{N_2} = 50$ mTorr has a very profound effect on the film crystallinity. Fig. 6(b) is the XRD pattern collected for the film deposited at 850 °C. This film exhibits sharp, intense (h00) perovskite peaks in its XRD pattern; an increase of 50 °C in the deposition temperature caused a great improvement in film crystallinity/orientation. A further increase in the deposition temperature to 900 °C (Fig. 6(c)) resulted in a film having a further increase (about 45%) in the observed intensity of the (200) peak, as compared to that for the film deposited at 850 °C. Thus, low N_2 pressures combined with higher deposition temperatures leads to excellent, singly oriented, perovskite(100) thin films on the single crystal $SrTiO_3(100)$ substrate. The out-of-plane lattice parameter, corresponding to $d_{(100)}$ interplanar spacing, is calculated to be 4.032 Å and is slightly larger than the $d_{(100)}$ value of 4.024 Å observed for the bulk [15]. As will be seen later, this out-of-plane tensile strain is the result of the substrate-induced in-plane compressive strain (the lattice parameters of the substrate are 2.96% smaller than those of bulk $SrNbO_3$).

For films grown on $SrTiO_3(110)$ crystals shown in Fig. 6(d) and (f), again the substrate peaks are marked s, and the film peaks can be indexed on the basis of singly-oriented perovskite $SrNbO_3(110)$ film. In contrast to growth on $SrTiO_3(100)$ substrates, all the films on $SrTiO_3(110)$ substrates exhibit sharp intense peaks (marked (hh0)); no dependence of the peak intensity on the growth temperature is observed. The $d_{(110)}$ interplanar spacing is calculated to be 2.861 Å and is slightly larger than the $d_{(110)}$ value calculated for the bulk [15]. As for the [100]-oriented films, the out-of-plane tensile strain is the result of the substrate-induced in-plane compressive strain, discussed later.
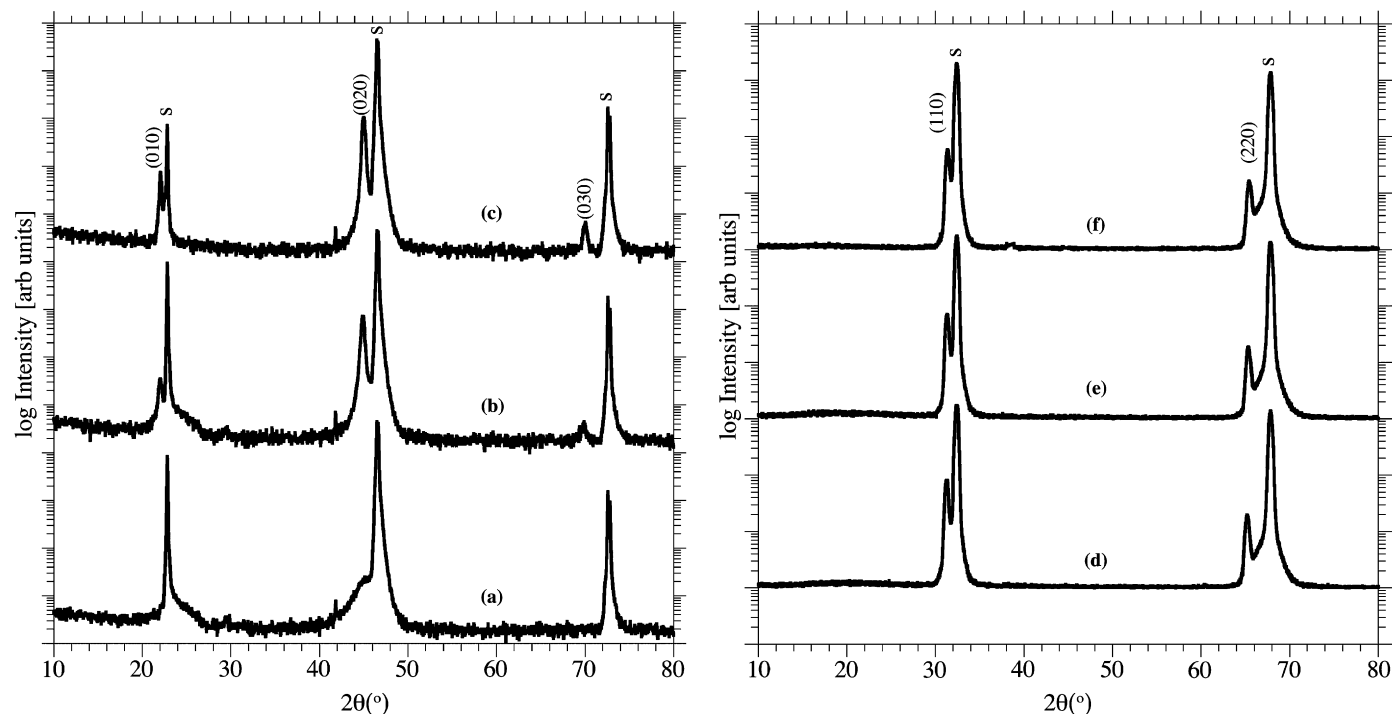
Fig. 6. XRD patterns of SrNbO$_3$ thin films deposited on treated (a–c) SrTiO$_3$(100) and (d–f) SrTiO$_3$(110) substrates. The films were deposited at $p_{N_2} = 50$ mTorr, and three different temperatures: 800, 850, and 900 °C; s denotes the substrate peaks. Only the (h00) reflections from the film on SrTiO$_3$(100) and only the (hh0) reflections from the film on SrTiO$_3$(110) are observed.

3.2.2. XRD-epitaxy

The epitaxial relationship between the SrNbO$_3$ film and the SrTiO$_3$ substrates was determined by registering azimuthal ϕ scans, and by comparing the locations in ϕ-space of the SrNbO$_3$ with the SrTiO$_3$ reflections. Fig. 7(a) is an overlay of the two {101} ϕ scans of the (100)-oriented substrate (marked SrTiO$_3$) and (100)-oriented film (marked SrNbO$_3$), although it should be noted that they were acquired at different 2θ angles ($2\theta = 32.45°$ for SrTiO$_3$ {110} and $2\theta = 31.51°$ for SrNbO$_3$ {110}). The observed four-fold intensity of the SrNbO$_3$ {110} suggests that there is a single in-plane texture. This indicates that the perovskite SrNbO$_3$ {110} peaks are aligned exactly with the SrTiO$_3$ {110} peaks in ϕ-space. Thus, the epitaxial relationship is determined to be: {100}$_{SrNbO_3}$||{100}$_{SrTiO_3}$; $\langle 110 \rangle_{SrNbO_3} \langle 110 \rangle_{SrTiO_3}$. From the 2θ positions of these peaks, the d-spacing of the (110) planes is 2.837 Å. Combined with the lattice spacing along the [100] direction of 4.032 Å, this gives an in-plane lattice parameter of 3.993 Å. The in-plane lattice parameter is smaller than the out-of-plane perovskite lattice parameter, i.e., the films are tetragonally distorted. The diffraction results also indicate that the films are not fully strained. The in-plane lattice parameter is 3.993 Å, which is neither the expected value for the bulk (4.024 Å [15]) nor the expected value of for a fully strained film (3.905 Å, which is the lattice parameter of the substrate).

Fig. 7(b) is a similar overlay of the ϕ scans of the {100} reflections of a (110)-oriented SrNbO$_3$ film with the {100} reflections of the (110)-oriented SrTiO$_3$ substrate. They were acquired at different 2θ angles ($2\theta = 44.94°$ for SrNbO$_3$ {100} and $2\theta = 46.46°$ for SrTiO$_3$ {100}). The observed two-fold intensity of the SrNbO$_3$ {100} suggests that there is a single in-plane texture. Again, the ϕ scans indicate that the perovskite SrNbO$_3$ {100} peaks are aligned exactly with the SrTiO$_3$ {100} peaks in ϕ-space giving an epitaxial relationship of: {110}$_{SrNbO_3}$||{110}$_{SrTiO_3}$; $\langle 1\bar{1}0 \rangle_{SrNbO_3}$||$\langle 1\bar{1}0 \rangle_{SrTiO_3}$. From the 2θ positions of these peaks, the d-spacing of the (100) planes is 4.026 Å. Combined with the lattice spacing along the [110] direction of 2.861 Å, this gives an in-plane d-spacing along the [1$\bar{1}$0] direction of 2.832 Å. Again, as in the case of growth on SrTiO$_3$(100) substrates, the SrNbO$_3$ film is under a compressive in-plane stress. The diffraction results also indicate that the films are partially relaxed. The in-plane $d_{1\bar{1}0}$ spacing is 2.832 Å, which is neither the expected value for the bulk (2.851 Å [15]) nor the expected value of for a fully strained film (2.761 Å, which is the $d_{1\bar{1}0}$ corresponding to the substrate).

3.2.3. Film morphology—AFM

Fig. 8 presents the AFM images for SrNbO$_3$ films deposited at two different temperatures of (a) 850 °C and (b) 900 °C on SrTiO$_3$(100) substrates (at a $p_{N_2} = 50$ mTorr for 30 min). The surface morphology of the perovskite films also exhibits an island-like morphology. However, compared to the Sr$_2$Nb$_2$O$_7$ films, the surface roughness of the SrNbO$_3$ films is an order of magnitude lower. Also, in this case, increasing the temperature does not have a significant effect on the surface roughness. These observations can be
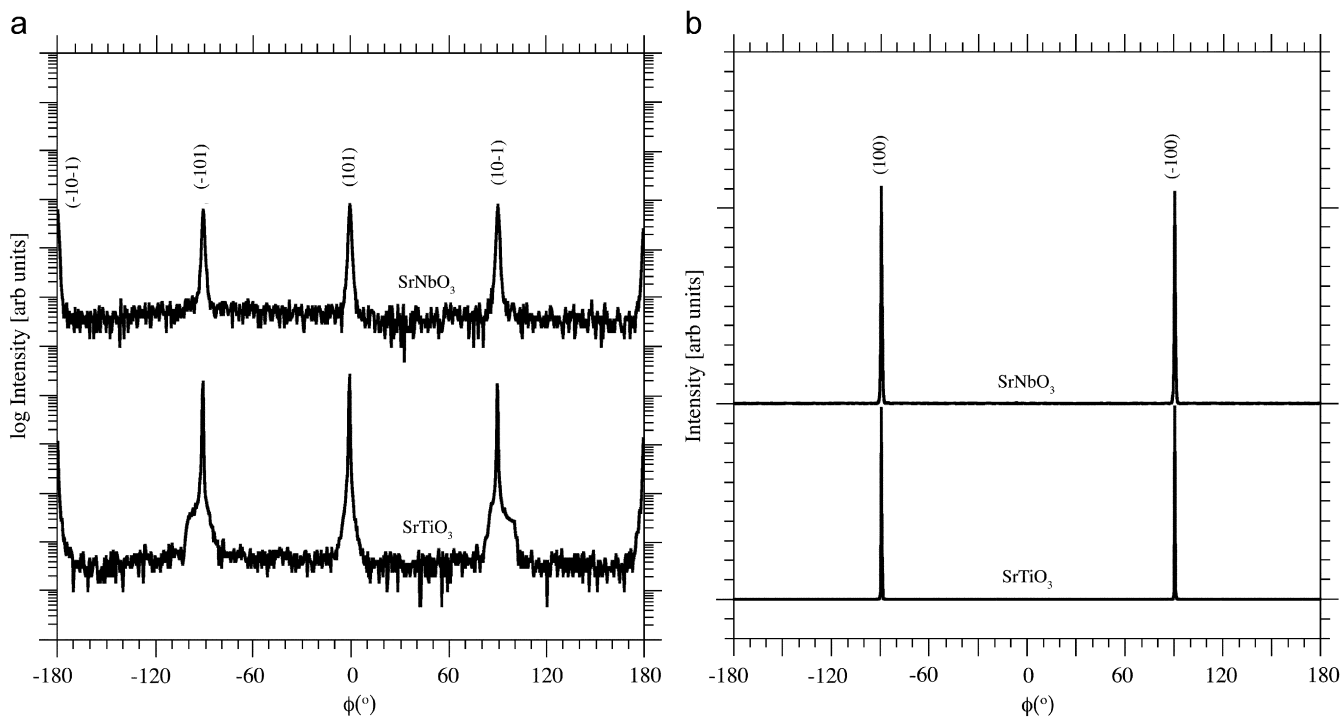
Fig. 7. (a) Azimuthal ϕ scans of the (101) reflection from the film (upper graph) and the substrate (lower graph). The film was deposited on $SrTiO_3$(100) at 850 °C and 50 mTorr N_2. (b) Azimuthal ϕ scans of the (100) reflection from the film (upper graph) and the substrate (lower graph). The film was deposited on $SrTiO_3$(110) at 850 °C and 50 mTorr N_2.
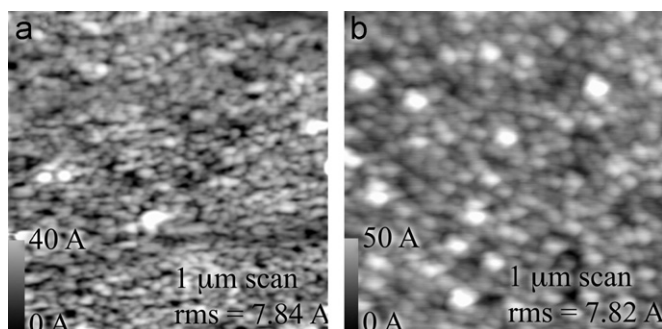

Fig. 8. AFM images of $SrNbO_3$ thin films grown on single crystal $SrTiO_3$(100) substrates in $p_{N_2} = 50$ mTorr and at (a) 850 °C and (b) 900 °C. The rms roughness values are ≈ 0.78 nm for both the films.

attributed to the fact that $SrNbO_3$ adopts a much simpler perovskite structure (compared to the complex layered structure of $Sr_2Nb_2O_7$), which is also very closely related to the crystal structure of the $SrTiO_3$ perovskite substrate.

3.2.4. TEM

Two aspects of the films obtained in N_2 atmospheres could not be resolved on the basis of X-ray data alone. First, even though the X-ray peaks from the film in Fig. 6 were attributed to the $SrNbO_3$ phase, this is not unambiguous. These peaks could as well be indexed on the basis of $SrNbO_2N$ [32,33], provided, nitrogen incorporation into the anion sublattice occurred because of deposition in nitrogen ambients. Both $SrNbO_3$ and

$SrNbO_2N$ adopt similar structures with similar lattice parameters [15,32]. Second, determination of the cation stoichiometry is also important; previous reports indicate that the stoichiometric $SrNbO_3$ compound is difficult to form in the perovskite structure [15,34,35]; the formation of the perovskite structure for this material is usually accompanied by a Sr-deficiency. EDS and selected area diffraction (SAD) on local regions in a TEM were used to address these issues.

Fig. 9(a) shows the image of the $SrNbO_3$ film on a $SrTiO_3$(100) substrate taken in STEM mode. The EDS scan given in Fig. 9(b) shows the elemental X-ray intensity of Sr, Nb, Ti, O, and N as a function of the distance along the line AB of length 80 nm in Fig. 9(a). The EDS data shows that the nitrogen signal (solid line, filled squares) is negligible and constant, scanning from the substrate to the film. This indicates that the nitrogen content of the film and substrate are approximately equal and, more importantly, that there exists only a very small, trace amount of nitrogen. Based on these observations, we can rule out the formation of the $SrNbO_2N$ phase when depositing in nitrogen atmospheres.

The signal from Sr is represented by the dotted line in Fig. 9(b), with the data points represented by the solid inverted triangles, and in the same figure the signal from oxygen is represented by solid line with filled circles. The observations of a constant Sr and oxygen signal are consistent with the fact that Sr and oxygen are present in both the film and substrate, at nominally the same levels for $SrTiO_3$ and $SrNbO_3$. The signal from Ti is high in the
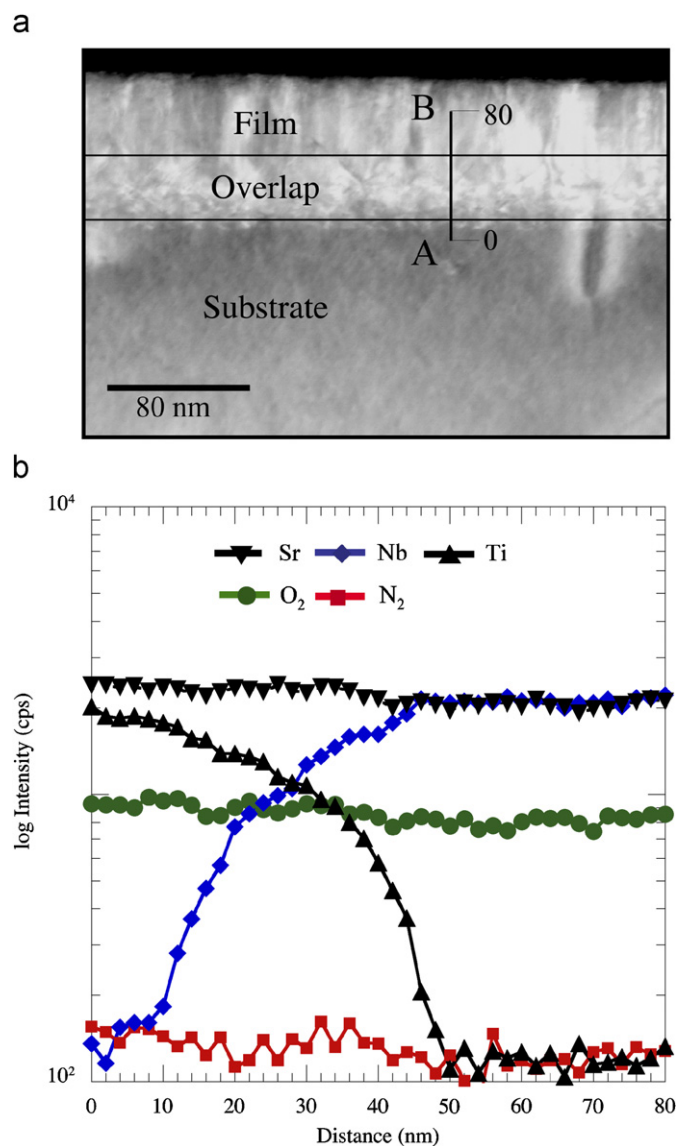
Fig. 9. (a) STEM image of the $SrNbO_3$ film on $SrTiO_3$ substrate. This area of the sample was used to collect the EDS line scan shown in Fig. 9(b). The line scan range of 80 nm is marked in this figure. (b) Results of the XEDS line scan plotted as the elemental X-ray intensity as a function of the distance along the line marked in Fig. 9(a). The overlap region where the signal from substrate and film overlap is also marked. The legend for the different elemental signals from the different elements of the substrate and film is also shown.
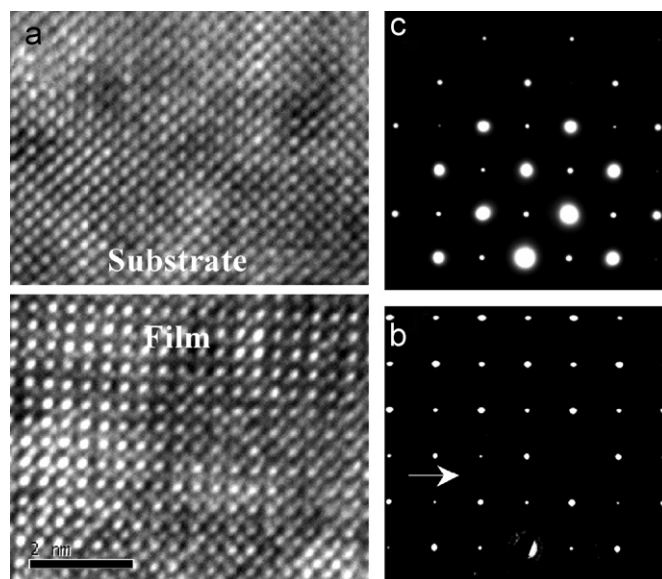

Fig. 10. (a) High-resolution TEM bright field image of the film–substrate interface for the $SrNbO_3$ film on $SrTiO_3(100)$ substrate. The solid white line in the figure marks the abrupt, high-quality interface between film and substrate. (b) Selected-area diffraction pattern from the film, corresponding to the $\langle 100 \rangle$-zone axis of cubic $SrNbO_3$. The arrow points to a position where one expects a superstructure reflection in the case of an orthorhombic distortion. (c) Selected-area diffraction pattern corresponding to the $\langle 100 \rangle$-zone axis of $SrTiO_3$ substrate.

substrate, and decreases to zero in the film. Likewise, the Nb signal is zero in the substrate, and increases to a maximum in the film. However, the signal from these two elements is not a step function; the overlap region shows signal from both Nb and Ti. This overlap region is seen owing to the geometry of the EDS experiment and not owing to interdiffusion. Furthermore, a quantitative analysis of the cationic ratios yielded a Sr:Ti ratio in the substrate of 1:1, and a Sr:Nb ratio in the film of 1:1. Collectively, these results imply that ablation of a $Sr_2Nb_2O_7$ target in a N_2 ambient leads to the formation of a stoichiometric $SrNbO_3$ film.

Fig. 10(a) is a high-resolution TEM bright field image of the film–substrate interface, showing an abrupt, high-quality, epitaxial interface. Fig. 10(b) and (c) shows the results of the companion selected area diffraction (SAD) study of the film and substrate, respectively. The patterns can be indexed on the basis of a simple perovskite cell. All the spots in the ED pattern of Fig. 10(c) correspond to the $\langle 100 \rangle$-zone axis of the cubic $SrTiO_3$. All the spots in the ED pattern of Fig. 10(b) can also be indexed either to a simple perovskite or on the basis of an orthorhombic unit cell, which is the reported form for the $SrNbO_3$ phase; the tetragonal distortion of the $SrNbO_3$ film obtained from the XRD patterns is too small to be revealed by the SAD patterns. In the orthorhombic setting, the spots in the ED pattern belong to the $\langle 101 \rangle$-zone axis. However, the orthorhombic modification should exhibit extra spots in the ED pattern (superstructure reflections). The absence of these superstructure reflections (the arrow points to one of the positions where the superstructure reflections are to be expected) implies that the $SrNbO_3$ film does not adopt the orthorhombically distorted perovskite structure but instead adopts a cubic perovskite structure (which is slightly tetragonally distorted owing to substrate induced stresses).

Fig. 11 is a low-resolution bright field image of the $SrNbO_3$ film whose SAD pattern was shown in Fig. 10. The bottom of the image corresponds to the region near the substrate. A significant amount of planar faults are observed in the image, seen as lines lying at 45° to the substrate planes. These stacking faults are attributed to extra O_2 planes lying perpendicular to the (110) habits,
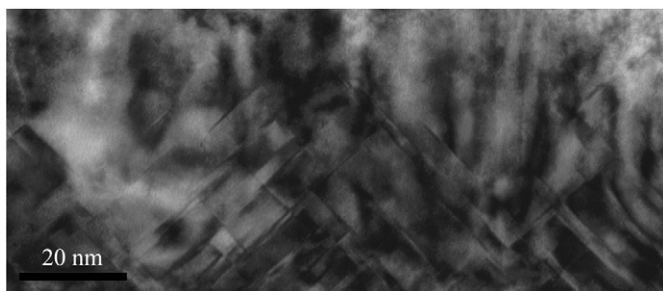
Fig. 11. Low-resolution bright field image of the SrNbO$_3$ film whose SAD pattern was shown in Fig. 10(b). A significant amount of planar faults are observed at the bottom of the image corresponding to the region near the substrate.

similar to the structural planes in Sr$_2$Nb$_2$O$_7$. These stacking faults have been previously observed in SrNbO$_3$ films deposited in much lower pressures. This implies that the Nb^{5+} is not fully reduced to Nb^{4+}.

3.2.5. Growth on other substrates

Fig. 12 shows the XRD patterns of films deposited for 1 h in a nitrogen ambient ($p_{N_2} = 200$ mTorr) and at $T_s = 850\,°C$. The substrate peaks are marked s on all four patterns in Fig. 12. Four different types of single-crystals were used as substrates in this experiment: (a) MgO(111), (b) MgO(100), (c) SrTiO$_3$(100), and (d) LaAlO$_3$(100)$_{pc}$. The film peaks could be indexed well to the reflections corresponding to SrNbO$_3$ (peaks marked (hkl)). On MgO(111), all the diffraction peaks that can be attributed to the film have low intensities. The film grows with a (100) texture. However, weak intensities from the (110), (220), and (111) perovskite reflections are also observed. (100)-oriented SrNbO$_3$ films were obtained on MgO(100) substrates too. Similar to the growth on MgO(111), weak intensity peaks that can be indexed as (110), and (220) perovskite reflections are also observed. On both SrTiO$_3$(100) and LaAlO$_3$(100)$_{pc}$, epitaxial (100)-oriented SrNbO$_3$ films are obtained.

Thus, independent of the orientation of the rock salt substrate, a (100) textured film is observed. The observation that the film grows as a cubic perovskite in a polycrystalline fashion on MgO(111) and MgO(100), which leads to semi-coherent and incoherent interfaces, respectively (with a mismatch of $\approx 4.45\%$), argues that the reduced perovskite phase is the stable phase in these deposition conditions. In other words, the perovskite is not a metastable product that is formed through epitaxial stabilization on an isostructural substrate, but is the preferred product in these absolute thermodynamic conditions. Though the substrate is not playing an important role in phase selection, it is playing a role in crystal quality and orientation selection.

4. Conclusions

The results presented conclusively demonstrate that the choice of the ambient gas is the major factor determining the
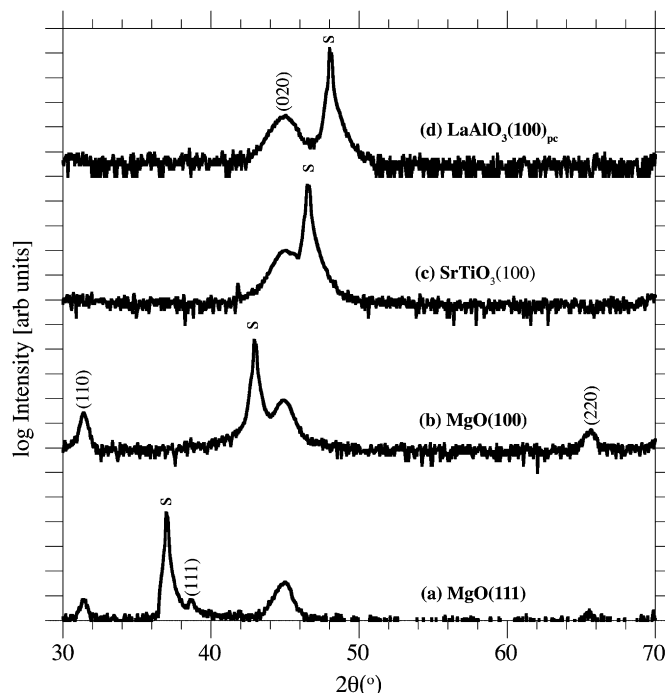

Fig. 12. XRD patterns of the SrNbO$_3$ perovskite thin films deposited on rock salt [MgO(111) and MgO(100)] and perovskite [SrTiO$_3$(100) and LaAlO$_3$(100)$_{pc}$] single crystal substrates. The films were deposited in $p_{N_2} = 200$ mTorr at 850 °C. Peaks labeled with an "s" denote substrate reflections while peaks labeled with (hkl) values denote film reflections.

phase selection between Sr$_2$Nb$_2$O$_7$ and SrNbO$_3$. Deposition from a Sr$_2$Nb$_2$O$_7$ target in oxygen atmospheres resulted in the formation of Sr$_2$Nb$_2$O$_7$ thin films on perovskite SrTiO$_3$(110) substrates. Deposition from the same Sr$_2$Nb$_2$O$_7$ target in nitrogen atmospheres resulted in the formation of the pure perovskite oxide SrNbO$_3$ on perovskite SrTiO$_3$ substrates. The films deposited on SrTiO$_3$(110) substrates in oxygen atmospheres ($p_{O_2} = 1$ mTorr) showed a preference for (001) orientation at lower temperatures. (010)-oriented films were preferred at higher temperatures. Variations in the oxygen pressure at high temperatures did not affect greatly the preference of an (010) oriented film, but X-ray intensities improved at lower pressures. More importantly, deposition from the same target, but in a N$_2$ ambient resulted in the formation of perovskite SrNbO$_3$ films. High-quality epitaxial films grew on perovskite SrTiO$_3$ substrates. The XEDS data showed that nitrogen incorporation into the anion sublattice was small and that the reduction of Nb^{5+} to Nb^{4+} occurred by changing the oxygen activity from O$_2$ to N$_2$. The preference to form the reduced perovskite phase in nitrogen ambients is evinced in the growth of SrNbO$_3$ films grow on MgO single crystal substrates albeit in a polycrystalline fashion.

References

[1] A.S. Bhalla, R. Guo, R. Roy, Mater. Res. Innovat. 4 (2000) 3.
[2] K. Akihiko, H. Kato, S. Nakagawa, J. Phys. Chem. B 105 (2000) 571–575.

[3] Y. Fujimori, T. Nakamura, A. Kamisawa, IEEE Trans. (1998) 55–58.
[4] A. Ishitani, M. Kimura, Appl. Phys. Lett. 29 (1976) 289–291.
[5] K. Okuwada, S. Nakamura, H. Nozawa, J. Mater. Res. 14 (1999) 855–860.
[6] M.A. Osman, A.K. Zeinally, N.N. Lebedeva, S.M. Efendiev, M. Grandolfo, P. Vecchia, Ferroelectrics 38 (1981) 861–863.
[7] A.V. Prasadrao, U. Selvaraj, S. Komarneni, J. Mater. Res. 10 (1995) 704.
[8] A.S. Neto, Acta Cient. Venezolano 31 (1980) 4–7.
[9] M. Shoyama, A. Tsuzuki, K. Kato, N. Murayama, Integr. Ferroelectr. 25 (1999) 195–203.
[10] S.Y. Stefanovich, S.S. Malhasyan, N.Y. Venevtsev, Ferroelectrics 29 (1980) 59–62.
[11] E.A. Wood, Acta Crystallogr. 4 (1951) 353.
[12] R.S. Roth, J.L. Waring, J. Res. Natl. Bureau Standards 65A (1961) 337.
[13] R. Marchand, F. Pors, Y. Laurent, Revue Internationale des Hautes Temperatures et des Refractaires 23 (1986) 11.
[14] M. Weiden, A. Grauel, J. Norwig, S. Horn, F. Steglich, J. Alloys Compd. 218 (1995) 13.
[15] D. Ridgley, R. Ward, J. Am. Chem. Soc. 77 (1955) 6132–6136.
[16] N. Ishizawa, F. Marumo, T. Kawamura, M. Kimura, Acta Crystallogr. B 31 (1975) 1912–1915.
[17] M. Jansen, H.P. Letschert, Nature 404 (2000) 980.
[18] N. Ishizawa, F. Marumo, T. Kawamura, M. Kimura, Acta Crystallogr. B 32 (1976) 2564.
[19] P.M. Gasperin, Acta Crystallogr. B 31 (1975) 2129–2130.
[20] T. Tomio, H. Miki, H. Tabata, T. Kawai, S. Kawai, J. Appl. Phys. 76 (1994) 5886–5890.
[21] S. Nakamatsu, M. Kimura, T. Kawamura, J. Phys. Soc. Jpn. 38 (1975) 817–824.
[22] N.A. Zakharov, V.A. Klyuev, Y.P. Toprov, V.P. Orlovskii, Inorg. Mater. 31 (1995) 1010–1012.
[23] J. Kim, S.I. Kwun, J.G. Yoon, J. Kor. Phys. Soc. 32 (1998) S1810.
[24] S. Takeno, R. Ohara, K. Sano, T. Kawakubo, Surf. Interface Anal. 35 (2003) 29.
[25] A. Perrone, Jpn. J. Appl. Phys. Part 1 41 (2002) 2163–2170.
[26] Y.-I. Kim, W. Si, P.M. Woodward, E. Sutter, S. Park, T. Vogt, Chem. Mater. 16 (2007) 618–623.
[27] K.R. Balasubramanian, A.A. Bagal, O. Castillo, A.J. Francis, P.A. Salvador, Ceram. Trans. 162 (2004) 59.
[28] J.L. Giocondi, A.M. Zimbouski, G.S. Rohrer, Mater. Res. Soc. Symp. Proc. 755 (2002) 221–226.
[29] A.J. Francis, A.J. Koritnik, A. Gellman, P.A. Salvador, Surf. Sci. 601 (2007) 1930–1936.
[30] M. Badaye, F. Wang, Y. Kanke, K. Fukushima, T. Morishita, Appl. Phys. Lett. 66 (1995) 2131–2133.
[31] F.M. Granozio, M. Salluzzo, U. Scotti di Uccio, I. Maggio-Aprile, O. Fischer, Phys. Rev. B 61 (2000) 756–765.
[32] S.G. Ebbinghaus, A. Weidenkaff, A. Rachel, A. Reller, Acta Crystallogr. C 60 (2004) i91–i93.
[33] Y.-I. Kim, P.M. Woodward, K.Z. Baba-Kishi, C.W. Tai, Chem. Mater. 16 (2004) 1267.
[34] H. Hannerz, G. Svensson, S.Y. Istomin, O.G. D'yachenko, J. Solid State Chem. 147 (1999) 421–428.
[35] N. Peng, J.T.S. Irvine, A.G. Fitzgerald, J. Mater. Chem. 8 (1998) 1033–1038.